

Optimal Synthesis of Stabilizer Codes via MaxSAT

Keyi Yin¹, Hezi Zhang¹, Yunong Shi², Travis Humble³, Ang Li⁴, and Yufei Ding¹

¹University of California, San Diego, CA, USA

²Amazon Braket, New York, NY, USA

³Oak Ridge National Laboratory, Oak Ridge, TN, USA

⁴Pacific Northwest National Laboratory, Richland, WA, USA

Abstract—Quantum Error Correction (QEC) codes are crucial for achieving fault-tolerant quantum computing in the long term. However, efficiently implementing these codes on hardware poses significant challenges, including hardware connectivity matching, efficient circuit scheduling, and fault-tolerance enforcement. In this study, we present an optimal synthesizer that stitches generic stabilizer codes onto diverse hardware structures via MaxSAT. Our evaluation demonstrates (1) the capability of our approach to be applied for various codes and devices and (2) the consistently better efficiency than the best prior heuristic approaches that only target specific QEC codes. By bridging the gap between high-level QEC code design and low-level hardware constraints, this work paves the way toward achieving long-term fault-tolerant quantum computing goals. We will open-source our code and provide the GitHub link in the final version.

I. INTRODUCTION

In recent years, the field of quantum computing has witnessed a rapid scale-up in hardware capabilities. For instance, IBM has achieved an impressive milestone of 400+ qubits [1], with plans to surpass 1000+ qubits in 2023 [2]. To unleash the full potential of quantum computation, quantum error correction (QEC) for fault tolerance has become the next frontier in the pursuit of "quantum supremacy" [3], [4]. Notably, significant strides have been made in recent QEC experiments, showcasing the implementation of logical operations on a distance-2 surface code [5], the performance improvement by scaling a surface code from distance 3 to 5 [6], and the realization of real-time QEC beyond break-even [7].

Among the diverse range of QEC codes, stabilizer codes stand out as an essential class encompassing a vast majority of known quantum codes [8], [9]. These codes possess distinct mathematical structures, such as the Abelian group [10] property, which facilitate the construction of encoding, decoding, and error-correction procedures [11], [12]. Various stabilizer codes, including the repetition code [13], Steane code [14], and surface code [15], [16], [17], have been developed to advance theoretical aspects, such as achieving higher error thresholds [18], [19], [20]. However, early efforts in their design largely overlooked the constraints imposed by the underlying hardware [21], [22], especially the limited qubit connectivity. This oversight has led to a substantial gap between theoretical design and practical realization, significantly impacting the effectiveness and efficiency of these codes in achieving large-scale, fault-tolerant quantum computing [23].

One recent effort by Anbang et al. [24] represents an initial step towards bridging the code-architecture gap. Notably, they address the challenge of mapping surface code [15], [16], [17], which is traditionally believed to require square architectures, onto sparser quantum architectures, such as heavy hexagons and heavy squares. The automatic framework is built on a clever exploitation of the unique characteristic of the surface code. Specifically, it takes advantage of the fact that all X- or Z-stabilizers in surface codes connect to four data qubits, leading to a uniform 2-D stabilizer layout. Their framework correspondingly starts by embedding the sparsely-connected coupling graph into a virtual 2D grid. Subsequently, it performs a search on this grid to identify "rectangles" that satisfy the 4-degree stabilizer layout. However, it should be noted that this approach is limited to stabilizer circuits structured as "rectangles" on the embedded grid, making it challenging to generalize to other stabilizer codes lacking this feature. Moreover, due to its heuristic nature, the method may not always guarantee to find the optimal solution.

Our ambitious goal is to create a framework that can effectively handle a wide range of stabilizer codes, going beyond the limitations imposed by specific circuit structures [25] or architectures [26]. In our initial investigation, this task may seem like a mission impossible, as different stabilizer codes often present varying numbers and structures of stabilizers [27]. These individual stabilizers also act on different data qubits and involve varying numbers of them, lacking specific structure information to capitalize on. Additionally, diverse fault-tolerant syndrome extraction methods [28], [29], [30] contribute to the complexity of the code synthesis problem.

The good news is that our further investigation reveals that while finding universal heuristics to leverage the intrinsic structure of diverse codes can be challenging, constraints-based optimizations [31], [32] provide a systematic and rigorous means to guide the synthesis process and explore the larger solution space. By treating each stabilizer as a syndrome extraction circuit that satisfies constraints for mapping data and ancilla qubits [33], [34], and viewing the stabilizer code as the co-mapping and co-scheduling of these individual stabilizers synergistically, we aim to devise a versatile and powerful framework to tackle the code-architecture gap in quantum computing. In addition to its versatility, the constraint-based approach offers the potential for optimality in synthesizing stabilizer codes.

We further illuminate the primary challenges in bridging the code-architecture gap, each of which will be addressed by formulating them as a set of constraints. **Connection Disparity:** Densely interconnected stabilizer measurement circuits clash with sparsely connected quantum hardware, hindering direct execution on the hardware. Addressing this requires thoughtful mapping of data and syndrome qubits, along with allocating additional ancilla qubits to resolve the connection mismatch. **Co-Scheduling Complexities:** Co-scheduling different stabilizer measurements presents a barrier to achieving the ideal assumption of full parallelism when these measurements are scheduled separately. This challenge arises from both the shared ancilla qubits, resulting in *incompatible* stabilizers that cannot be executed in parallel, and the shared data qubits, necessitating a proper arrangement of gate orders within the circuit to ensure the measurement correctness. **Fault-Tolerant Execution:** Achieving fault-tolerant execution of stabilizer measurement circuits proves intricate due to error propagation from two-qubit gates. While various studies [26], [35], [36] delve into the error-correction scheme with the potential for fault-tolerance, they often come with the trade-off of introducing additional constraints on the stabilizer circuits.

To this end, we propose CodeStitch, a novel constraint-based approach for fault-tolerant stabilizer code synthesis. Our approach formulates and solves the synthesis task as a two-stage optimization problem based on MaxSAT [32]. The first stage focuses on stabilizer mapping to address the *connection disparity* challenge, while the second stage involves stabilizer operation scheduling to resolve *co-scheduling complexities*. In the **stabilizer mapping** stage, we tackle the issue of limited hardware connectivity by mapping each data qubit to a physical qubit and each syndrome qubit to a connected block of ancilla qubits adjacent to the data qubits. This is achieved through a SAT-encoded breadth-first traversal (BFT) algorithm [37]. The goal is to minimize the *CNOT* gate number and maximize the compatibility between stabilizers, reducing ancilla qubit overhead and enabling parallel scheduling in the next stage. In the **stabilizer scheduling** stage, we optimize the parallelism of stabilizer measurement circuits by scheduling each stabilizer as a five-phase circuit and enforcing pipeline constraints to address conflicts between stabilizers and ensure measurement correctness. We use an iterative query to the SAT solver, gradually increasing the circuit depth limit in each iteration until a solution is found. To meet the **fault-tolerance** requirement, we add scheme-specific constraints in both stages. For generic stabilizer codes, we adopt Shor’s scheme [28] as the default measurement scheme. Alternatively, if fault-tolerance is guaranteed by an elaborate manual design of stabilizer circuits [26], [35], [38], we can accommodate them by imposing their design-specific constraints.

Overall, we make the following contributions:

- We identify and formulate three critical challenges for implementing generic stabilizer codes on the underlying hardware with diverse coupling structures, including hardware constraints, efficient circuit scheduling, and fault-tolerance enforcement.

- We tackle these challenges by proposing a constraint-based approach, which systematically formulates the synthesis problem of stabilizer codes as a two-stage MaxSAT problem and efficiently explores the vast optimization space with the state-of-the-art MaxSAT solver.
- Our evaluation demonstrates the versatility of our framework across a range of stabilizer codes and device architectures, as well as its optimality to significantly enhance fidelity when compared to heuristic approaches.

II. BACKGROUND AND MOTIVATION

In this section, we provide an introduction to stabilizer codes and shed light on the challenges encountered when synthesizing them on quantum hardware through examples.

A. Stabilizer Codes

Stabilizer codes are essential quantum codes [39] represented through the stabilizer formalism [40]. An $[[n, k, d]]$ stabilizer code stores k logical qubits in n data qubits, with d denoting the minimum number of physical qubits required to convert codewords. Stabilizer codes use $n - k$ stabilizers, each represented by a tensor product of Pauli operators P . The weight of a stabilizer generator is defined as $wt(s_k) = \text{count}(P_i \neq I)$, which represents the number of qubits it needs to operate on.

$$\begin{aligned} Stabs &= \{s_1, s_2, \dots, s_{n-k}\} \\ s_k &= P_1 P_2 \dots P_n, \text{ where } P_i \in \{I, X, Y, Z\} \end{aligned}$$

A codeword is stabilized by all the stabilizers of the code, implying it is a simultaneous eigenstate of all stabilizers with an eigenvalue of $+1$ [39]. By checking this “stabilizing” property, stabilizer codes enable the detection and correction of errors in a quantum system. The set of all such legitimate states forms the codespace. For the codespace to be non-trivial, all stabilizers (also known as generators) of the codespace must commute with each other, forming an Abelian group [40].

B. Error Syndrome Extraction Circuits

The *error syndrome extraction circuit* is used to measure whether the input quantum state is an eigenstate of a stabilizer with an eigenvalue of $+1$. Fig. 1(b) depicts such a circuit for measuring the stabilizer $s = X_a X_b X_c X_d$. The measurement outcome of the syndrome qubit (*i.e.*, *error syndrome*) reveals whether an error has occurred on data qubit, assuming the original quantum state is a valid codeword.

While this measurement scheme is effective in theory, it may fail to meet the specific hardware constraints and account for detailed error propagation toward fault-tolerant execution.

Connection Disparity. Using a single syndrome qubit for stabilizer measurement, as shown in Fig. 1, requires the ancilla qubit to connect to all data qubits the stabilizer operates on. This necessitates mapping it to a physical qubit with at least $wt(s)$ neighboring qubits. However, real quantum devices [2] lack such highly-connected qubits. For example, the latest IBM quantum device [1] exhibits a heavy hexagonal structure with nodes having only degrees of 2 and 3, posing challenges for direct circuit mapping due to connectivity limitations.

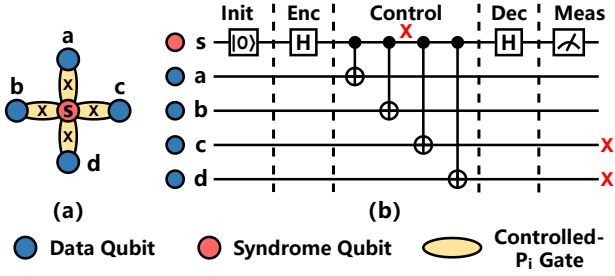


Fig. 1. Error syndrome extraction circuit for stabilizer X_{abcd} with a single syndrome qubit. (a) The stabilizer structure. (b) The syndrome extraction circuit. A single fault X_s after the second $CNOT$ gate could result in the correlated 2-qubit error X_cX_d on the data qubits, which is possibly uncorrectable.

Fault-Tolerant Execution. Moreover, the measurement circuit depicted in Fig. 1 can potentially raise fault-tolerant concerns. If an X error occurs on the syndrome qubit after the first two $CNOT$ gates, it can propagate onto two data qubits c and d . This correlated error, denoted as X_cX_d , may share the same error syndrome as some single-qubit errors in certain low-distance QEC codes. For example, in a stabilizer code with $d = 3$, this two-qubit error could surpass the error correction capability of the code. Consequently, in the next round of syndrome measurements, a single-qubit error might be misidentified instead of the original two-qubit error, resulting in a logical qubit error.

An Example that Resolves Both Concerns. Fig. 2 depicts a fault-tolerant syndrome extraction circuit for the stabilizer $s = X_aX_bX_cX_d$. It is both fault-tolerant and requires only a block of syndrome qubits with degrees 2 and 3. We provide a simple example to illustrate the fault tolerance of this scheme. If an X error occurs on ancilla qubit s_3 just before the last $CNOT$ gate in the *Encoding* phase, it will propagate to the correlated error X_cX_d on data qubits. However, this X error will also cause the multi-qubit error $X_{s_1}X_{s_2}Z_{s_3}$ after the *Decoding* phase, resulting in both Z measurements on s_1 and s_2 returning non-trivial result 1 during the *Measurement* phase. With this additional information, we can diagnose the error X_cX_d . The method we employ here for ensuring fault tolerance is also referred to as Shor’s scheme [28]. For more details about the error decoding and correction, we recommend reference [41].

A Five-Stage Circuit Pipeline Abstraction. Indeed, we observe that any error syndrome extraction circuit $Circuits[s_k]$ of a stabilizer s_k can be represented as a five-stage pipeline, *Initialization*, *Encoding*, *Control*, *Decoding*, and *Measurement*:

$$Circuits[s_k] = \text{Init}[s_k] \cup \text{Enc}[s_k] \cup \text{Ctrl}[s_k] \cup \text{Dec}[s_k] \cup \text{Meas}[s_k]$$

In particular, the interaction between ancilla qubits and data qubits happens in the *Control* phase through controlled- P_i gates. We denote these gates as $ctrl(P_i, s_i, q_i)$, where ancilla qubit s_i is the control qubit, data qubit q_i is the target qubit, and P_i is the Pauli operator of the stabilizer s_k acting on q_i . Since CY and CZ gates can be transformed into CX (i.e., $CNOT$) gates

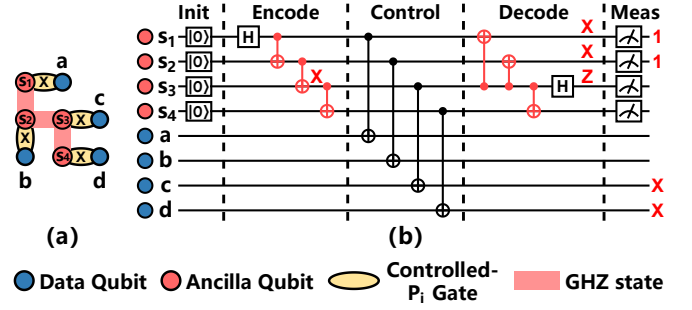


Fig. 2. Error syndrome extraction circuit for stabilizer X_{abcd} with a block of ancilla qubits under Shor’s fault-tolerant measurement scheme [28]. (a) The stabilizer structure, with ancilla qubits in red forming a block, and yellow edges indicating controlled- P_i gates (CX for X_{abcd}). (b) The five-phase syndrome extraction circuit. The red X and Z letters indicate a possible error propagation, with red 1s representing the measurement return a non-trivial result.

with single-qubit gates, we use $CNOT$ gates to denote general controlled- P_i gates in the paper.

C. Error Syndrome Extraction Scheduling

This section focuses on the key challenges of co-scheduling all stabilizer measurements in a stabilizer code. The pipelined view of each individual error syndrome extraction circuit provides a foundation for circuit scheduling. However, co-scheduling multiple stabilizers can be significantly more complex. We will now highlight two key challenges in this context.

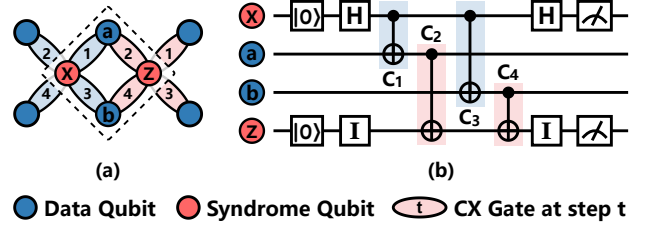


Fig. 3. Surface code stabilizers with S-shaped order of $CNOT$ gates. (a) Structure of two adjacent X and Z stabilizer. (b) Circuit to measure the operators X_aX_b and Z_aZ_b in the dashed box. The two identity I operators on syndrome qubit Z are performed to ensure that the measurement timing of two stabilizer matches.

Shared Ancilla Qubits: Error syndrome extraction circuit for stabilizer with shared ancilla qubits may not be able to execute in parallel. For example, since the qubit s in Fig. 1 is occupied throughout all the five stages, circuits for any other stabilizers would have to wait if they also need to utilize this qubit. This significantly affect the latency of the QEC circuit since most syndrome extraction circuits would require highly connected ancilla qubits similar to s . To maximize the parallelism, we would prefer different stabilizers to acquire non-overlapping qubits, for which case we say their circuits are *compatible*.

Shared Data Qubits: Error syndrome extraction circuit for stabilizer with common data qubits need to follow appropriate orders to ensure the correctness of the syndrome extraction. Otherwise, the final measurements will just return random results. For example, as demonstrated in Fig. 3, in the surface

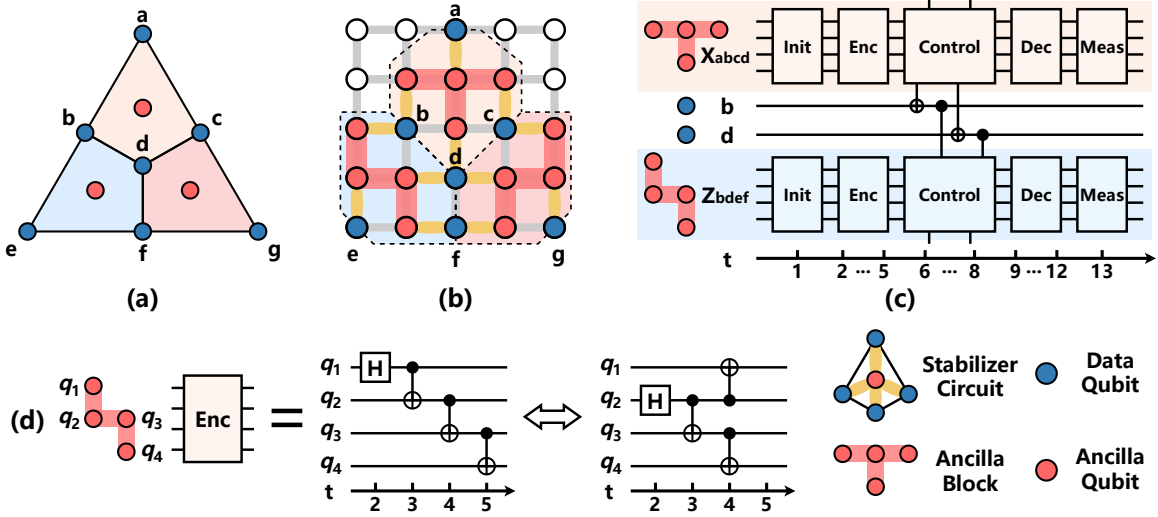


Fig. 4. Synthesizing Steane Code (a) by mapping the qubits onto a 5×5 square lattice (b) and scheduling the syndrome extraction circuits with 5 phases (c). Data qubits are depicted in blue and ancilla qubits are depicted in red, with the ancilla qubits of each stabilizer in (b) forming an ancilla block. Syndrome extraction circuits of X_{abcd} and Z_{bdef} are scheduled concurrently in (c), with the gate order managed appropriately in the Control phase. The scheduling process can be affected by different ways of preparing GHZ states on ancilla blocks, with (d) showing two equivalent circuits of preparing GHZ states on the S-shaped ancilla block.

code setup, the order of $CNOT$ gates is important. The X- and Z-type stabilizers must adhere to a specific sequence: either a Z-shaped pattern ($C_1 \rightarrow C_3 \rightarrow C_2 \rightarrow C_4$) or an S-shaped pattern ($C_1 \rightarrow C_2 \rightarrow C_3 \rightarrow C_4$) [35]. Deviating from this proper order, such as in a clock sequence ($C_2 \rightarrow C_1 \rightarrow C_3 \rightarrow C_4$), will lead to the measurement of operators $X_a X_b X_c$ and $Z_x Z_a Z_b$ instead of the intended $X_a X_b$ and $Z_a Z_b$ [42].

III. OVERVIEW

In this section, we present an example of applying CodeStitch to synthesize the Steane Code onto a 2-D grid hardware, as shown in Fig. 4. The example focuses on providing an overview of CodeStitch, especially inputs/outputs in different stages. Detailed technical aspects are in Section IV.

A. Overview of Stage 1: Stabilizer Mapping

Input1: Our first input is the stabilizer code to be synthesized. The stabilizer code is encoded as a list of Pauli operator strings. For instance, the $[[7, 1, 3]]$ Steane code, whose code layout is depicted in Fig. 4(a), can be encoded as follows:

$$\text{Stabs} = \left\{ \begin{array}{lll} X_a X_b X_c X_d, & X_b X_d X_e X_f, & X_c X_d X_f X_g, \\ Z_a Z_b Z_c Z_d, & Z_b Z_d Z_e Z_f, & Z_c Z_d Z_f Z_g \end{array} \right\}$$

For simplicity, we will use the notations s_1 to refer to the first stabilizer $X_a X_b X_c X_d$ and s_i to denote the i th stabilizer.

Input2: Our second input is the quantum hardware to be deployed. We adopt a general device coupling graph, $\text{Graph} = (\text{Phys}, \text{Edges})$, to encode the coupling constraints on the quantum hardware. Here $\text{Phys} = \{p_1, p_2, \dots\}$ denotes the set of physical qubits, and $\text{Edges} = \{e_1, e_2, \dots\}$ represents the set of direct physical coupling between the physical qubits. Fig. 4(b) illustrates a device with 25 physical qubits, forming a 5×5 squared lattice. The edges between qubits indicate whether we

can perform two-qubit operations between them. For example, we can perform a controlled-Z gate directly over $p_{1,1}$ and $p_{1,2}$, but not between $p_{1,1}$ and $p_{2,2}$. We also use $\text{Adj}(p_i)$ to represent all the physical qubits that are adjacent to p_i .

Output: The output of Stage 1 comprises three parts, as shown in Fig. 4(b). ① *Data qubits mapping* (in blue), $\Pi: \text{Data} \rightarrow \text{Phys}$, e.g., $\Pi(a) = p_{1,3}$ and $\Pi(b) = p_{3,2}$. ② *Ancilla block allocation* (in red), $\text{Anc}: \text{Stabs} \rightarrow P[\text{Phys}]$, where $P[\text{Phys}]$ stands for a collection of physical qubits. We allow partial/exact overlapping between ancilla blocks of different stabilizers, e.g., $\text{Anc}[s_1] = \text{Anc}[s_4] = \{p_{2,2}, p_{2,3}, p_{2,4}, p_{3,3}\}$. ③ *Coupling relation* between data qubit and ancilla qubit (yellow edges), $\text{CP}: \text{Stab} \times \text{Data} \rightarrow \text{Phys}$, indicating which ancilla qubit of the stabilizer is used to couple with the data qubit, e.g., $\text{CP}(s_1, a) = p_{2,3}$ and $\text{CP}(s_2, e) = p_{4,1}$.

B. Overview of Stage 2: Stabilizer Scheduling

Stage 2 exclusively takes inputs from the outputs derived from Stage 1. Its outputs encompass 1) the error syndrome extraction circuits for all stabilizers and 2) the corresponding time schedule of each gate within these circuits. Fig. 4(c) provides an example output for the Steane Code, with only the co-scheduling of s_1 and s_5 plotted out and the detailed gates within the circuits omitted for simplicity. We next provide more details about these two outputs.

Output 1: Syndrome extraction circuit for each stabilizer s . The five stages of the circuit are treated separately. For $\text{Init}[s]$, $\text{Ctrl}[s]$, and $\text{Meas}[s]$, circuits can be determined using the output from Stage 1. For instance, in the *Control* phase of stabilizer $s_1 = X_a X_b X_c X_d$, the required gates between ancilla and data qubits can be deduced from the *coupling relation*, i.e., $CNOT$ gates between all pairs of qubits connected by yellow edge for s_1 in Fig. 4(b), such as that between data qubit

a and ancilla qubit $p_{2,3}$. In contrast, for $Enc[s]$ and $Dec[s]$, circuits exist design flexibility. As shown in Fig. 4(d), multiple circuit options are equivalent for preparing the GHZ state on the S-shaped ancilla block during the *Encoding* phase of s_5 , each employing distinct sets of gates and requiring different length of time. For further information, please refer to Section 4.2.

Output 2: Time schedule of each gate. With the syndrome extraction circuits for each stabilizer s obtained in Output 1, this step further determines the co-scheduling of all stabilizers. The time schedule can be represented as a mapping from all gates in the circuits to time steps: $Circuits \rightarrow \{1, 2, 3, \dots\}$. For any gate $g \in Circuits$, its time coordinate is denoted as t_g . In Fig. 4(c), the time axis illustrates the time slots assigned to each of the five phases of the syndrome extraction circuits, such as time steps 2-5 for the *Encoding* phase. For further clarity, Fig. 4(d) provides comprehensive details about the gates scheduled at different time slots in the *Encoding* phase.

C. Overview of Fault Tolerance Schemes

We embrace Shor’s scheme [28] as our default fault-tolerance approach due to its broad applicability. As elaborated in section II, this scheme only requires the straightforward and code-agnostic GHZ state $|+\rangle_{Anc[s]} + |-\rangle_{Anc[s]}$ in the *Encoding* phase and the transversal *CNOT* gate in *Control* phase. These requirements can be introduced as special fault-tolerant constraints in our synthesizer.

In addition to Shor’s scheme, we also accommodate different manual designs of fault-tolerant error syndrome extraction circuits for some specific QEC codes, such as the surface code [35] and the flag-bridged Steane Code [38]. These designs possess certain mapping of qubits and order of operations, which can be introduced as additional constraints in our synthesizer.

IV. CONSTRAINT-BASED STABILIZER CODE SYNTHESIS

In this section, we delve into the technical details of the two stages in CodeStitch: stabilizer mapping and scheduling.

A. Stage 1: MaxSAT Encoding of Stabilizer Mapping

In this stage, we encode the mapping problem of data qubits and ancilla blocks into a MaxSAT problem. We formulate the qubit position constraints as hard constraints, and formulate the objectives of minimizing total ancilla block size and incompatible stabilizer count as soft constraints, denoted as (*Hard*, *Soft*). The so Additionally, we incorporate extra hard constraints based on the measurement scheme to fulfill the fault-tolerance requirement.

1) Variables:

Boolean variables: We use the following Boolean variables, matching the three outputs of stage 1 as described in section III:

① $map(q, p)$: Indicates the mapping of data qubit q to physical qubit p in Π . For example, in Fig. 4(b), the data qubit a is mapped to $p_{1,3}$, which is represented by $map(a, p_{1,3}) = True$.

② $anc(s, p)$: Denotes the allocation of ancilla qubits for stabilizer s . For instance, in Fig. 4(b), the allocation $p_{2,4} \in Anc[s_1]$ is represented by $anc(s_1, p_{2,4}) = True$.

③ $cp(s, q, p)$: Represents the coupling relation of stabilizer s between data qubit q and physical qubit p . For example, in Fig. 4(b), both $cp(s_1, a, p_{2,3})$ and $cp(s_5, b, p_{3,1})$ are assigned a value of *True*, indicating the coupling between the data qubit that the stabilizer acts on and its corresponding ancilla qubit.

Other Variables: We introduce additional variables to address performance concerns for the solver. These variables represent the upper bound size of the ancilla block for each stabilizer $s \in Stabs$, denoted as $L[s]$. In Fig. 4, for example, we have $L[s_1] = \dots = L[s_6] = 4$. Setting $L[s]$ to $|Phys|$ avoids a maximum size constraint, but a smaller bound improves the MaxSAT solver’s efficiency.

To optimize resource usage and solver performance, we iteratively set the upper bound size $L[s]$ for each stabilizer $s \in Stabs$. Initially, $L[s]$ is set to the lower bound based on the measurement scheme: $wt(s)$ for Shor’s scheme and 1 for the partial Flag-Bridge scheme. If the MaxSAT solver returns “UNSATISFIABLE” or fails to find a solution within a limited time, we increment each $L[s]$ by 1 to explore a larger search space. This iterative refinement finds suitable sizes for ancilla blocks that yield better results.

2) Hard Constraints:

Hard A. Injective data qubit mapping. This set of constraints ensures that the map variables represent an injective function, meaning that each data qubit is mapped to a unique physical qubit:

$$\begin{aligned} \sum_{p \in Phys} map(q, p) &= 1, \text{ for } q \in Data \\ \sum_{q \in Data} map(q, p) &\leq 1, \text{ for } p \in Phys \end{aligned}$$

These constraints can be encoded by the exactly-one (EO) and at-most-one (AMO) encoding [43], which use $O(n)$ auxiliary variables consisting a “ladder” to propagate the information of *True* value between all the n variable in the summation.

Hard B. No ancilla-data mapping collision. This set of constraints ensures that a physical qubit $p \in Phys$ cannot serve as both a data qubit and an ancilla qubit simultaneously:

$$\neg map(q, p) \vee \neg anc(s, p), \text{ for } q, s \in Data \times Stabs$$

Hard C. Maximum size for ancilla blocks. This set of constraints guarantees that an ancilla block $Anc[s]$ is allocated at most $L[s]$ ancilla qubits. To achieve this, we introduce auxiliary boolean variables $A(k, s, p)$, where $k \in \{1, \dots, L[s]\}$. It is set to *True* only when the k -th ancilla qubit of $Anc[s]$ is mapped to physical qubit p :

$$anc(s, p) \leftrightarrow \bigvee_{1 \leq k \leq L[s]} A(k, s, p)$$

Thus, the “at-most- N ” constraint can be encoded into N at-most-one constraints:

$$\sum_{p \in Phys} A(k, s, p) \leq 1, \text{ for } s \in Stabs \text{ and } k \in \{1, \dots, L[s]\}$$

Since ancilla qubits are not required to be mapped to unique physical qubits, it's possible for some of them to overlap on the device, resulting in an ancilla block with a size smaller than $L[s]$.

Hard D. Connectivity of ancilla block. This set of constraints guarantees that each mapped ancilla block forms a connected graph. Connectivity of induced subgraph $Graph[Anc[s]]$, which consists of all qubits in $Anc[s]$ and associated edges between them, ensures the preparation of the ancilla state on the block.

To encode the connectivity constraint of $Anc[s]$ with Boolean variables $anc(s, p)$, we employ the idea of breadth-first traversal (BFT) [37]. Given that $|Anc[s]| \leq L[s]$, all the physical qubits in $Graph[Anc[s]]$ can be visited within a maximum of $L[s]$ time steps. To represent the traversal of $Graph[Anc[s]]$ starting from physical qubit p , we introduce auxiliary variables $v_{s,p}(p_i, t)$, where $p_i \in Phys$ and $t \in \{1, \dots, L[s]\}$. The variable $v_{s,p}(p_i, t)$ indicates whether the physical qubit p_i has been visited after t -th round. In the initial round, we only visit the starting vertex p :

$$v_{s,p}(p, 1) \bigwedge_{p_i \neq p} \neg v_{s,p}(p_i, 1)$$

In the t -th round of the traversal, a unvisited physical qubit $p_i \in Anc[s]$ will be visited if and only if at least one of its adjacent qubits $p_j \in Adj(p_i)$ has been visited in the previous $t - 1$ rounds:

$$v_{s,p}(p_i, t) \rightarrow anc(s, p_i) \wedge \left[v_{s,p}(p_i, t-1) \vee \bigvee_{p_j \in Adj(p_i)} v_{s,p}(p_j, t-1) \right]$$

Since the specific physical qubits that belong to $Anc[s]$ and can serve as the starting point for the Breadth-First Search (BFS) are undecided, it becomes necessary to enforce constraints for every $p \in Phys$, requiring that:

$$anc(s, p) \rightarrow \bigwedge_{p_i \in Phys} (\neg anc(s, p_i) \vee v_{s,p}(p_i, L[s]))$$

Hard E. Coupling between data qubits and ancilla block. This set of constraints ensures that each data qubit for stabilizer s is physically connected directly to some ancilla qubits in the ancilla block $Anc[s]$. Specifically, it enforces the following conditions:

1) Exactly one ancilla qubit p is used to be coupled with data qubit q :

$$\sum_{p \in Phys} cp(s, q, p) = 1, \text{ for } q \in Data[s]$$

2) The coupling relation $CP(s, q) = p$ requires q to be mapped to some qubits p_i adjacent to p :

$$cp(s, q, p) \rightarrow \bigvee_{p_i \in Adj(p)} map(q, p_i) \bigwedge anc(s, p)$$

Hard F. Fault tolerance constraints: transversal CNOT gates. This set of constraints ensures that the synthesized stabilizer code satisfies the requirements of our default measurement

protocol, Shor's scheme [28], meaning that all the *CNOT* gates in the *Control* phase are transversal on the ancilla block. In other words, in any stabilizer s , there is at most one *CNOT* gate $g_i \in Ctrl[s]$ on each ancilla qubit $p \in Anc[s]$:

$$\sum_{q \in Data[s]} cp(s, q, p) \leq 1, \text{ for } s \in Stabs \text{ and } p \in Phys$$

Nevertheless, in the case of other manually designed stabilizer codes, constraints might be different. For example, the flag-bridge scheme [38] requires that each ancilla block must contain at least one flag qubit, denoted by the condition $|Anc[s]| \geq 2$.

If *Hard F* is excluded from the set of hard constraints, we refer to this measurement scheme as the "partial flag-bridge". The term "partial" is used because this scheme can be viewed as a hybrid approach, combining elements from both the bare ancilla and flag-bridge schemes.

3) *Soft Constraints:*

We next introduce a set of soft constraints to optimize the performance of synthesized stabilizer code. Each soft clause will be assigned a non-negative weight to indicate its priority. With a MaxSAT solver, we can obtain a solution that maximizes the combined weight of the satisfied soft clauses.

Soft P1. Minimizing the total ancilla block size. This set of constraints ensures the measurement circuit remains small, as a larger circuit tends to be more error-prone. Since the ancilla block for a stabilizer s can be represented as $\{p \in Phys \mid anc(s, p) = True\}$, minimizing the total ancilla block size is equivalent to maximizing the number of Boolean variables $anc(s, p)$ that are set to *False*. Thus, we add the following soft constraints assigned with weight *P1*:

$$\neg anc(s, p), \text{ for } s, p \in Stabs \times Phys$$

Soft P2. Mitigating the stabilizer conflicts. This set of constraints ensures that the mapped stabilizers can be efficiently executed in parallel. Stabilizers s and s' can be measured concurrently only if their corresponding ancilla blocks do not overlap. Stabilizers that meet this condition are considered compatible. Therefore, our objective is to maximize the count of compatible ancilla block pairs. Thus, we introduce the following soft constraints assigned with weight *P2*:

$$\bigwedge_{p \in Phys} \neg anc(s, p) \vee \neg anc(s', p), \text{ for } s, s' \in Stabs$$

In Fig. 5, we present the impact of diverse measurement schemes and optimization objectives on the resulting mappings. We illustrate four different mappings of the code $Stabs = X_1 X_2 X_3, Z_2 Z_3$ to a heavy square architecture. In the second row, for instance, Soft P2 is chosen as the objective with first priority, indicating that the weight P_2 is significantly greater than P_1 . As shown in the table, varying the priority leads to different data qubit mappings and ancilla block allocations. As discussed in Section V, we generally prioritize the total size of ancilla blocks (P1) over the number of incompatible stabilizers (P2), as the former has a more significant impact on the overall error correction performance.

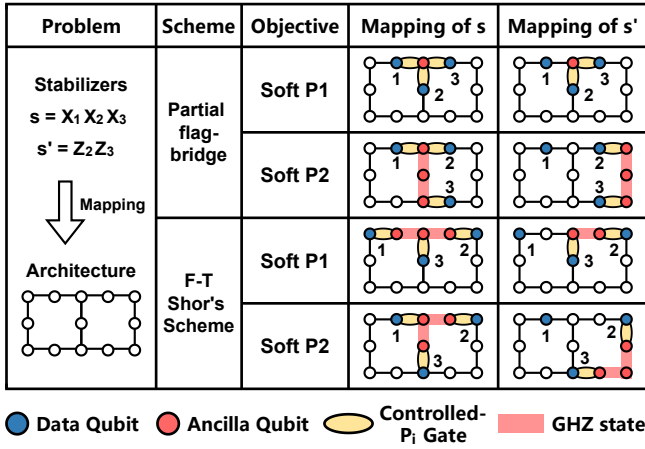


Fig. 5. Different mappings for stabilizer s and s' under different measurement schemes (partial flag-bridge vs. fault-tolerant Shor's scheme) and objectives (Soft P1: minimizing the total ancilla block size vs. Soft P2: mitigating the stabilizer conflicts).

B. Stage 2: SAT Encoding of Stabilizer Scheduling

In this stage, we formulate the scheduling problem of syndrome extraction circuits into a SAT problem. We identify all operations within the syndrome extraction circuits from the output of stage 1, and introduce constraints by analyzing the dependence of operations from the perspective of relations within or between the five phases of stabilizer.

1) Error Syndrome Extraction Circuits:

Before addressing scheduling, it is necessary to determine all the operations, which means to establish the set $Circuits$ from the results of the stabilizer mapping. As outlined in Section III, when considering a stabilizer s , only the operations in *Initialization*, *Control*, *Measurement* phases have been identified:

$$\begin{aligned}
 Init[s] &= \{init(p) \mid p \in Anc[s]\} \\
 Ctrl[s] &= \{ctrl(P_q, CP(s, q), \Pi(q)) \mid P_q \neq I \in s\} \\
 Meas[s] &= \{Mz(p) \mid p \in Anc[s]\}
 \end{aligned}$$

For the gates in *Encoding* and *Decoding* phases, if the H gate is treated as an *CNOT* with both control and target on itself, there is exactly one *CNOT* targeted at each ancilla qubit. So we can represent $Enc[s]$ and $Dec[s]$ as:

$$\begin{aligned}
 Enc[s] &= \{CX_e(p) \mid p \in Anc[s]\} \\
 Dec[s] &= \{CX_d(p) \mid p \in Anc[s]\}
 \end{aligned}$$

where $g = CX_{e(d)}(p)$ represent a *CNOT* gate with p as a target qubit in the *Encoding* (*Decoding*) phase, the control qubit $g.ctrl$ need to be determined in Stage 2.

2) Variables:

Boolean variables: We use the following Boolean variables, matching the two outputs of stage 2 as described in Section III:

① $enc(s, p, p')$ and $dec(s, p, p')$: Indicates the encoding and decoding circuits in $Enc[s]$ and $Dec[s]$. For example, consider Fig. 4(d), in the left circuit design of $Enc[s_5]$, a *CNOT* gate

is applied from q_1 to q_2 , represented by $enc(s_5, q_1, q_2) = True$. This indicates that $CX_e(q_2).ctrl = q_1$.

② $time(g, t)$: Denotes the time assignment of operations g in the entire $Circuits$. For instance, in Fig. 4(d), in the right circuit design of $Enc[s_5]$, a *CNOT* gate $g = CX_e(q_3)$ is executed at time step 2, which is represented by $time(g, 2) = True$.

Other variables: We introduce additional variable T to represent the upper limit of time steps, with t ranging in $\{1, 2, \dots, T\}$. To find a depth-optimal solution, the scheduler engages in an iterative process that queries the SAT solver repeatedly to determine if it is possible to schedule the syndromes extraction circuit within an overall circuit depth less than T . If the result is "UNSATISFIABLE", T will be augmented by multiplied with a factor $\epsilon > 1$.

3) Hard Constraints:

In this sections, we will present a comprehensive outline of our constraints from four perspectives: time assignment constraints, within-phase constraints, between-phase constraints and fault-tolerant constraints.

1) Time Assignment Constraints:

Hard A. All operations are executed. Since each operation can only be mapped to one time slot, indicating that exactly one element in the set $\{time(g, t) \mid t \in \{1, \dots, T\}\}$ will be assigned the *True* value in the solution:

$$\sum_t time(g, t) = 1, \text{ for } g \in Circuits$$

Hard B. No operation collision. To prevent collision of operations, we enforce that if two operations g and g' act on the same physical qubit, they cannot be executed at the same time. In other words, for any physical qubit p , at most one operation acting on p can be executed at time t :

$$\sum_{g \in Act[p]} time(g, t) \leq 1, \text{ for } t \in \{1, \dots, T\}$$

where $Act[p]$ denotes all the operations that act on p . If the operation is not determined but has the potential to act on p , i.e. $g = CX_e(p')$ when $p \in Anc[s]$, $time(g, t)$ will be replaced by $time(g, t) \wedge enc(s, p, p')$.

2) Within-Phase Constraints:

Hard C. Valid $Enc[s]$ and $Dec[s]$ circuits. This set of constraints ensures that the circuits in the *Encoding* phase and *Decoding* phase can function as the encoding and decoding of a GHZ state. In the *Encoding* phase, an ancilla qubit p can only be prepared after an H gate or a *CNOT* gate controlled by another prepared ancilla qubit targeting p . If the H gate is treated as visiting the root node and $CNOT(p_i, p_j)$ is treated as visiting p_j through the edge (p_i, p_j) , $Enc[s]$ can be considered as a transversal starting at the root of the tree on $Anc[s]$. In other words, whether $Enc[s]$ and $Dec[s]$ are valid circuits is equivalent to $Enc[s]$ and the mirror of $Dec[s]$ forming a tree transversal. The following parts outline the constraints for $Enc[s]$, while a similar formulation can be applied to $Dec[s]$.

(1) The transversal tree has exactly one root, which means only the root ancilla qubit have $CX_e(\text{root}) = H$:

$$\sum_{p \in \text{Anc}[s]} \text{enc}(s, p, p) = 1$$

(2) Each node within the transversal is visited exactly once, ensuring that every ancilla qubit $p \in \text{Anc}[s]$ is subjected to exactly one $CNOT$ gate targeting it:

$$\sum_{p_i \in \text{Anc}[s]} \text{enc}(s, p_i, p) = 1$$

(3) If $g_j = CX_e[p_j] = CNOT(p_i, p_j)$, it must be executed after p_i has been prepared. In other words, g_j must be executed after $g_i = CX_e[p_i]$:

$$\text{enc}(s, p_i, p_j) \rightarrow (t_{g_i} < t_{g_j}), \text{ for } p_i \neq p_j \in \text{Anc}[s]$$

Although the clause $t_{g_i} < t_{g_j}$ can be easily encoded by pairwise encoding when the upper bound T is given, we implement a ladder structure akin to that of AMO and EO encoding, which minimizes the total count of clauses.

Hard D. Correct order of $Ctrl[s]$ circuits. As discussed in Section II, the order of anti-commutable controlled- P_i gates in the *Control* phase affects the measurement property. In fact, the order is correct if and only if the count of anti-commutable gate pairs (c, c') satisfying $t_c < t_{c'}$ is an even number. This is due to the fact that two anti-commutable controlled- P_i gates together are commutable, allowing us to switch their order. The even number means that the order is equivalent to the trivial sequential order, which is always a correct order since it means that stabilizer s finishes before stabilizer s' begins. As a result, we enforce the constraint:

$$\bigoplus_{\text{Anti}(c, c')} (t_c < t_{c'}) = 0, \text{ for } c \in \text{Ctrl}[s] \text{ and } c' \in \text{Ctrl}[s']$$

where \bigoplus means the mod 2 addition and $\text{Anti}(c, c')$ means c and c' are anti-commutable. The mod 2 addition can also be encoded effectively by using the a ladder structure similar to those in AMO and EO encoding.

3) *Between-Phase Constraints:*

Hard E. Operation pipelining. For the five phases in a stabilizer, they must be executed in a strict sequential order, which means that operations in the succeeding phases must wait for the operations in the preceding phases to finish. Consequently, if $g \in \text{Phase}_i[s]$ and $g' \in \text{Phase}_{i+1}[s]$ act on the same qubit, we enforce the constraints $t_g < t_{g'}$.

Hard F. Incompatible stabilizers. When two stabilizer circuits, s and s' , have shared ancilla qubits, their ancilla states cannot exist simultaneously. This constrain can be realized by requiring $\text{Init}[s]$ after $\text{Meas}[s']$, $\text{Init}[s']$ after $\text{Meas}[s]$:

$$\left[\bigwedge_{p \in \text{Share}} (t_{Mz'[p]} < t_{\text{Init}[p]}) \right] \vee \left[\bigwedge_{p \in \text{Share}} (t_{Mz[p]} < t_{\text{Init}'[p]}) \right]$$

where $\text{Share} = \text{Anc}[s] \cap \text{Anc}[s']$ represent all physical qubit that shared by two stabilizer's ancilla block.

4) *Fault Tolerance Constraints:*

Hard H. Designed order of $Ctrl[s]$ circuits. This set of constraints is utilized to accommodate existing manually designed stabilizer code. Some manually designed code may have special execution order for the data-ancilla $CNOT$ gates in the *Control* phase. For instance, [44] proposed a fault tolerant syndrome extraction approach for $[[2^r - 1, 2^r - 1 - 2r, 3]]$ Hamming code, which have a permutation to reorder the CX or CZ gates in each stabilizer to make possible errors have distinct syndromes. Similarly, [35] improved stabilizer measurement circuits of surface code, where the X-type and Z-type stabilizer follows different measurement order. Based on these designed order of the $CNOT$ gates in the $Ctrl[s]$, we can create a directed graph to show the dependence between $CNOT$ gates, indicating which gates should be executed first. So for any direct edge (g, g') in the graph, we enforce the constraint $t_g < t_{g'}$.

V. IMPLEMENTATION AND EVALUATION

A. Experimental Setup

Evaluation setting: We use the state-of-the-art MAXSAT solver, NuWLS-c [45] and SAT solver, PySAT [46] for the synthesis problem, both with a time limit of 7,200 seconds for solving. The increment factor ϵ for T is designated as 1.3. The weight assigned to the Soft P1 clauses is determined as the total count of all Soft P2 clauses with a weight of 1. For error threshold and logical error analysis, we utilize stim [47], a fast stabilizer circuit simulator, and PyMatching [48], a decoder of Minimum Weight Perfect Matching (MWPM) algorithm, and general error model used in previous study [24], [42].

Hardware architectures: We use different device architectures to execute the stabilizer codes, showed in Fig. 6. To represent the connectivity limitations, we use the average degree denoted as $\text{Density}(G) = 2|\text{Edge}|/|\text{Phys}|$. The selected architectures are sourced from latest quantum machines, such as Google's Sycamore [4], IBM's Osprey and IBM Q Tokyo [1], with densities ranging from 2.4 to 6. We also choose alternative architectures with matching densities to investigate the impact of structural differences.

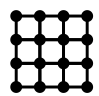
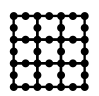
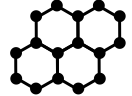
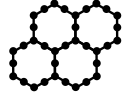
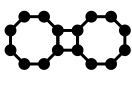
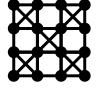
Name	Density	Arch Example	Name	Density	Arch Example
Square	4.00		Heavy Square	2.67	
Hexagon	3.00		Heavy Hexagon	2.40	
Octagon	3.00		Tokyo	6.00	

Fig. 6. Overview of device architectures.

Stabilizer codes: In our experiments, we synthesize a diverse set of stabilizer codes with distinct features, including classical codes such as the $[[9, 1, 3]]$ surface code and the $[[7, 1, 3]]$ Steane

code, color codes like the $[[16,4,3]]$ 2D color code and the $[[8,3,2]]$ 3D color code, as well as more generic non-CSS codes such as the five-qubit $[[5,1,3]]$ code. We select these codes for evaluation based on several reasons: 1) Many stabilizer codes can be seen as extensions or combinations of these foundational codes. For example, larger distance surface codes can be constructed from the 3-distance surface code [49], and the $[[22,4,3]]$ and $[[12,2,3]]$ color codes can be obtained by merging Steane codes [26]; 2) Code layout difference is considered by the synthesis of both 2D and 3D color codes onto the devices with 2D planar coupling graphs; 3) Synthesizing more generic codes is demonstrated through the case of the non-CSS five-qubit code, which is also the most dense code. The measurement scheme is also taken into account. We use the "Partial Flag-Bridge" scheme for the $[[16,4,3]]$ 2D color code and the $[[9,1,3]]$ surface code since they have special manual design where syndromes can be extracted fault-tolerantly without flag qubits. For the rest of the codes, we use Shor's scheme.

To quantify the level of interconnectivity for each stabilizer code, we define the density of a stabilizer code, denoted as $Density(C)$, as follows:

$$Density(C) = \frac{\sum_{s \in Stabs} wt(s)}{|Stabs| + |Data|}$$

Metrics: In this work, we consider three key metrics. First, we evaluate the *CNOT gate count* of the synthesized QEC codes to demonstrate the performance of the generated code. The high sensitivity to two-qubit gate errors in the stabilizer code makes the count of *CNOT* gates in the entire circuits a crucial factor that significantly affects the fidelity of syndrome extraction. Second, We assess the *Circuit Depth* of entire error syndrome extraction circuit, which is the maximum time coordinates of all operations. Due to the limitation of current quantum computing technology, physical qubits can only function well up to a short 'lifetime'. Thus, minimizing depth becomes crucial to ensure efficiency. A larger time-step count would introduce more decoherence errors that accumulate, eventually surpassing the fault tolerance threshold of the error correction procedure. Finally, we examine *Physical Qubit Count* to illustrate the resource overhead of the synthesized surface codes. Since real quantum devices only provide a finite number of physical qubits, for more logical qubits to be allocated, an efficient synthesis should utilize fewer qubits.

B. Synthesis of Various Stabilizer Codes

We begin by employing CodeStitch to synthesize a wide array of stabilizer codes and explore various architectures. The results are presented in Table I. The "Ideal" column is used as a baseline, which represents a fully-connected architecture. By comparing with the ideal situation, we discuss the influence of architecture and stabilizer code on the synthesized result. The "*" symbol following the number indicates that it represents a satisfactory (but not optimal) solution returned by the solver within the limited time allotted for computation.

The influence of architectures: (1) In general, high-density architectures are more effective for stabilizer code synthe-

sis compared to low-density architectures. When comparing hexagon architectures to square architectures, the former exhibits an average increase of 26.3% in the number of 2-qubit gates and an average increase of 47.9% in the circuit depth. (2) Density of the architecture is not the sole factor affecting synthesis. For example, in the synthesis of the $[[16,4,3]]$ code, transitioning from a hexagon architecture to an octagon architecture results in a significant increase in the number of 2-qubit gates, circuit depth, and the count of physical qubits cost. Despite both architectures having the same density of 3, the matching degree between the native stabilizer structure and the target architecture proves to be the key factor that impacts code synthesis. (3) Physical qubit requirements can sometimes be lower on sparse architectures compared to dense architectures. For example, with the $[[5,1,3]]$ code, the sparse Tokyo architecture requires 18 qubits, while the ideal architecture needs 31 qubits. This is because our solver prioritizes optimizing the number of *CNOT* gates during the synthesis process. Consequently, on a sparse architecture, it encourages extensive sharing between adjacent ancilla blocks, leading to a decrease in overall qubit usage. Yet, sharing reduces parallelism among the blocks, resulting in a higher circuit depth and diminishing overall error protection effectiveness.

The influence of stabilizer code: (1) In general, high-density code needs high-density architecture. For instance, $[[9,1,3]]$ surface code reach the ideal situation on Square while there is still optimization space for the $[[16,4,3]]$ color code on Square. (2) Stabilizer codes are influenced to varying degrees by architecture density, and there is an upper bound on architecture density that can substantially improve the performance and cost of stabilizer code synthesis. For instance, when comparing the $[[7,1,3]]$ Steane code synthesized on Square and Tokyo architectures, both demonstrate similar performance and cost, closely approaching the ideal situation. (3) It is not just the stabilizer code but also the specific fault-tolerance scheme used that can impact hardware requirements. For instance, when employing Shor's scheme-based synthesis, it guarantees transversal data-ancilla interaction, resulting in lower degree requirements for ancilla qubits and allowing near-optimal deployment on low-density architectures.

C. Compared to Heuristic Approach on Surface Code

We compared our Stab-Stitch approach with Surf-Stitch [24], a heuristic method proposed just for synthesizing surface codes. Fig. 7 gives error thresholds, which are calculated based on the synthesized surface codes at different distances, while Table II provides comprehensive details for the synthesized surface codes of distance 3.

Overall, our CodeStitch in Fig. 7 demonstrates consistently better error correction capabilities in all settings. In particular, we highlight the following four results.

(1) The primary metric influencing the error threshold is the count of *CNOT* gates. The substantial improvement in the threshold, observed in the Hexagon and Octagon architectures in Fig. 7, can be attributed to an approximate 30% reduction in the utilization of *CNOT* gates.

TABLE I
RESULTS OF CODESTITCH AND THE "IDEAL" BASELINE FOR VARIOUS STABILIZER CODES ACROSS DIFFERENT DEVICE ARCHITECTURES.

Code	Density	Arch		Ideal	Square	Hexagon	Octagon	H-Square	H-Hexagon	Tokyo
		Metrics								
[[7, 1, 3]] Steane Code	3.69	# <i>CNOT</i> gate		60	60	64	68	68	96	60
		Circuit depth		9	17	24	27	30*	30	17
		# physical qubit		31	19	20	19	19	25	19
[[16, 4, 3]] 2D Color Code	4.29	# <i>CNOT</i> gate		60	80	120	152	132	240*	76
		Circuit depth		10	17	18	24	26	30	19
		# physical qubit		28	27	37	44	37	61*	26
[[8, 3, 2]] 3D Color Code	3.69	# <i>CNOT</i> gate		62	62	66	66	76*	100	62*
		Circuit depth		11	20	31	31	30	33	19
		# physical qubit		32	26	16	16	24*	21	28*
[[5, 1, 3]] Five-Qubit Code	3.56	# <i>CNOT</i> gate		40	40	44	44	50	60	40
		Circuit depth		9	24	30	30	33*	32	16
		# physical qubit		31	15	10	10	11	12	18
[[9, 1, 3]] Surface Code	2.82	# <i>CNOT</i> gate		24	24	38	56	48	84	24
		Circuit depth		8	8	19	21	20	16	8
		# physical qubit		17	17	19	24	25	37	17

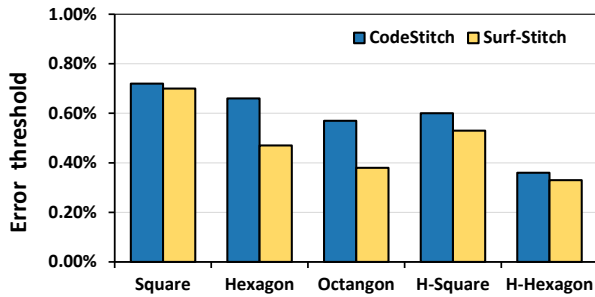


Fig. 7. Error threshold comparison of CodeStitch and Surf-Stitch on various architectures (A higher threshold implies a stronger error protection capability of the synthesized QEC code).

TABLE II

DETAILED INFORMATION ABOUT THE SYNTHESIZED SURFACE CODES.

Arch	Metrics		# <i>CNOT</i> gate	Circuit depth	# physical qubit
	CodeStitch	Surf-Stitch			
Square	CodeStitch		24	8	17
	Surf-Stitch		24	8	17
Hexagon	CodeStitch		38	19	19
	Surf-Stitch		60	26	21
Octagon	CodeStitch		56	21	24
	Surf-Stitch		80	28	27
Heavy Square	CodeStitch		48	20	25
	Surf-Stitch		48	24	25
Heavy Hexagon	CodeStitch		84	16	37
	Surf-Stitch		88	40	31

(2) When two synthesized circuits have an equivalent or nearly similar count of *CNOT* gates, circuit depth can also profoundly affect the error threshold. For instance, consider the comparison between CodeStitch and Surf-Stitch on the Heavy Square architecture, both employing the same surface code mappings. However, due to a more concurrent scheduling strategy, CodeStitch achieves a remarkable 0.07% increase in the error threshold by reducing 16.7% of circuit depth.

(3) An unapparent element influencing the error threshold, not presented in Table II, is the sequence in which measurements are conducted for *CNOT* gates. For instance, in comparison to Surf-Stitch on Square architecture, our synthesized code

exhibits a slightly higher threshold, despite both utilizing the same stabilizer mapping. This difference can be attributed to our incorporation of S2.Hard H, inspired by [35], to employ distinct measurement orders for X- and Z-type stabilizers. In contrast, Surf-Stitch only utilizes a consistent S-shaped order for both categories of stabilizers.

(4) While CodeStitch may require more qubits than Surf-Stitch in cases like Heavy Hexagon for parallel stabilizer mapping, this doesn't necessarily enlarge the total resource cost. Given the exponential impact of the error threshold on the logical error rate, it is worthwhile to trade increased qubit usage for reduced circuit depth in order to achieve a lower final cost of physical qubits while reaching the target logical error rate.

D. More Error Threshold Analysis

This study provides a breakdown analysis of how the error threshold shifts across two vital error types: two-qubit *CNOT* gate errors and device idle errors. The simulation focuses on surface codes on 2-D grid hardware, but the conclusion can be readily extrapolated to broader contexts. This analysis provides additional support for the rationale behind prioritizing the reduction of # *CNOT* gates (linked to accumulated *CNOT* errors) over circuit depth (linked to accumulated idle errors) when optimizing QEC code synthesis.

The results are shown in Figure 8. The figure highlights the *error threshold*, which is the convergence point of curves representing surface codes of different distances. When analyzing the two-qubit gate error, the idle error is set to 0, and vice versa. As shown, pure *CNOT* gate error exhibits a per-step threshold of 1.3%, while pure idle error showcases that of 3.1%. The much lower threshold for *CNOT* errors substantiates both the decreased tolerance for this type of error and its amplified impact on the ultimate logical error rate. This underscores the significance of prioritizing the objective of reducing the overall *CNOT* gate count within the circuits.

E. Scalability Discussion

Our empirical evaluation confirms the effectiveness of CodeStitch across a diverse set of generic stabilizer codes.

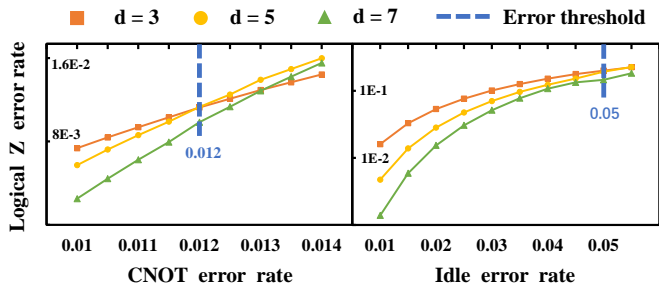


Fig. 8. Error Threshold Breakdown Analysis.

Our CodeStitch successfully finds optimal solutions for many of these QEC codes within the time limit and provides viable alternatives for others. We also observe that synthesis time is not solely determined by the scale of the code; the degree of mismatch between the code and architecture also significantly impacts it. For instance, synthesizing the $[[9, 1, 3]]$ surface code on a 2D lattice takes 2-3 minutes, while the $[[8, 3, 2]]$ code requires hours. The discrepancy arises because the mismatch introduces a substantial synthesis space to explore, making it challenging to find an optimal solution.

Looking ahead, we acknowledge the consideration surrounding the scalability of our framework, given the inherent challenges posed by the solver’s scalability. Nonetheless, we maintain optimism due to the potential of integrating these modestly-sized, generic codes toward a hierarchical QEC code synthesis approach. As such, we anticipate that upcoming innovations, especially the integration of heuristic slicing techniques, will significantly enhance CodeStitch’s capabilities, enabling its seamless application to more extensive scenarios.

VI. RELATED WORK

Manually designed QEC code implementation: Prior studies have proposed intricate fault-tolerant designs for specific codes, such as color code [26], surface code [35] or subsystem code [50]. However, these designs overlook connectivity constraints and make assumptions about the device’s ability to accommodate such designs. In [38], a flexible fault-tolerant circuit design was introduced, theoretically capable of accommodating diverse hardware structures. However, its focus remains at the individual circuit level and cannot be applied to solve the code-architecture gap, where interactions among different stabilizer circuits significantly complicate the design space. To bridge the code-architecture gap, specific QEC codes are still being manually designed [51]. For instance, in [25], stitched surface codes were introduced to address the requirements of heavy architecture devices.

Automatic Heuristic-based Approaches: Automating QEC code synthesis is still a new area with only some preliminary study. Recent study [24] employs heuristic methods to stitch surface codes onto various hardware structures. The automatically synthesized QEC codes from their framework demonstrate comparable or superior error correction capability to prior manually designed QEC codes [25]. However, these

heuristic-based approaches are specialized for surface codes, rendering lacking the extensibility to generic QEC codes.

VII. CONCLUSION

In this paper, we conduct a comprehensive analysis and in-depth discussion of the challenges for stitching generic stabilizer codes to diverse underlying hardware. We formulate the fault-tolerant stabilizer code synthesis as a MaxSAT problem and propose an optimal approach that solves the stabilizer mapping and scheduling tasks in two stages. By exploring a vast design and optimization space efficiently with the state-of-the-art MaxSAT solver, our framework demonstrates remarkable versatility across a range of stabilizer codes and device architectures, and reaches a consistently better efficiency than the circuits designed by code-specific heuristic approach.

VIII. ACKNOWLEDGMENTS

We thank the anonymous reviewers for their valuable and constructive feedback. This work was supported in part by NSF 2138437, NSF 2048144, and the Robert N. Noyce Trust.

REFERENCES

- [1] Jerry Chow, Oliver Dial, and Jay Gambetta. Ibm quantum breaks the 100-qubit processor barrier. *IBM Research Blog*, 2, 2021.
- [2] Jay Gambetta. Ibm’s roadmap for scaling quantum technology. *IBM Research Blog (September 2020)*, 2020.
- [3] Exponential suppression of bit or phase errors with cyclic error correction. *Nature*, 595(7867):383–387, 2021.
- [4] Frank Arute, Kunal Arya, Ryan Babbush, Dave Bacon, Joseph C Bardin, Rami Barends, Rupak Biswas, Sergio Boixo, Fernando GSL Brandao, David A Buell, et al. Quantum supremacy using a programmable superconducting processor. *Nature*, 574(7779):505–510, 2019.
- [5] JF Marques, BM Varbanov, MS Moreira, Hany Ali, Nandini Muthusubramanian, Christos Zachariadis, Francesco Battistel, Marc Beekman, Nadia Haider, Wouter Vlothuizen, et al. Logical-qubit operations in an error-detecting surface code. *Nature Physics*, 18(1):80–86, 2022.
- [6] Suppressing quantum errors by scaling a surface code logical qubit. *Nature*, 614(7949):676–681, 2023.
- [7] VV Sivak, Alec Eickbusch, Baptiste Royer, Shraddha Singh, Ioannis Tsioutsios, Suhas Ganjam, Alessandro Miano, BL Brock, AZ Ding, Luigi Frunzio, et al. Real-time quantum error correction beyond break-even. *Nature*, 616(7955):50–55, 2023.
- [8] Michael A Nielsen and Isaac L Chuang. *Quantum computation and quantum information*. Cambridge university press, 2010.
- [9] Ivan B Djordjevic. *Quantum information processing, quantum computing, and quantum error correction: an engineering approach*. Academic Press, 2021.
- [10] László Fuchs, JP Kahane, AP Robertson, and S Ulam. *Abelian groups*, volume 960. Springer, 1960.
- [11] Jean-Pierre Françoise, Gregory L Naber, and Sheung Tsun Tsou. *Encyclopedia of mathematical physics*, volume 2. Elsevier Amsterdam, 2006.
- [12] A Robert Calderbank, Eric M Rains, Peter M Shor, and Neil JA Sloane. Quantum error correction via codes over $gf(4)$. *IEEE Transactions on Information Theory*, 44(4):1369–1387, 1998.
- [13] Asher Peres. Reversible logic and quantum computers. *Physical review A*, 32(6):3266, 1985.
- [14] Andrew Steane. Multiple-particle interference and quantum error correction. *Proceedings of the Royal Society of London. Series A: Mathematical, Physical and Engineering Sciences*, 452(1954):2551–2577, 1996.
- [15] A Yu Kitaev. Quantum computations: algorithms and error correction. *Russian Mathematical Surveys*, 52(6):1191, 1997.
- [16] A Yu Kitaev. Quantum error correction with imperfect gates. In *Quantum communication, computing, and measurement*, pages 181–188. Springer, 1997.
- [17] A Yu Kitaev. Fault-tolerant quantum computation by anyons. *Annals of physics*, 303(1):2–30, 2003.

- [18] David K Tuckett, Stephen D Bartlett, and Steven T Flammia. Ultrahigh error threshold for surface codes with biased noise. *Physical review letters*, 120(5):050505, 2018.
- [19] Helmut G Katzgraber, Héctor Bombín, and Martin A Martin-Delgado. Error threshold for color codes and random three-body ising models. *Physical review letters*, 103(9):090501, 2009.
- [20] Daniel Crow, Robert Joynt, and Mark Saffman. Improved error thresholds for measurement-free error correction. *Physical review letters*, 117(13):130503, 2016.
- [21] Alysso Gold, Anna Stockklauser, Matt Reagor, Jean-Philip Paquette, Andrew Bestwick, Cody James Winkleblack, Ben Scharmann, Feyza Oruc, and Brandon Langley. Experimental demonstration of entangling gates across chips in a multi-core qpu. In *APS March Meeting Abstracts*, volume 2021, pages F30–007, 2021.
- [22] Eric J Zhang, Srikanth Srinivasan, Neereja Sundaresan, Daniela F Bogorin, Yves Martin, Jared B Hertzberg, John Timmerwilke, Emily J Pritchett, Jeng-Bang Yau, Cindy Wang, et al. High-fidelity superconducting quantum processors via laser-annealing of transmon qubits. *arXiv preprint arXiv:2012.08475*, 2020.
- [23] Gushu Li, Yufei Ding, and Yuan Xie. Towards efficient superconducting quantum processor architecture design. In *Proceedings of the Twenty-Fifth International Conference on Architectural Support for Programming Languages and Operating Systems*, pages 1031–1045, 2020.
- [24] Anbang Wu, Gushu Li, Hezi Zhang, Gian Giacomo Guerreschi, Yufei Ding, and Yuan Xie. A synthesis framework for stitching surface code with superconducting quantum devices. In *Proceedings of the 49th Annual International Symposium on Computer Architecture, ISCA '22*, page 337–350, New York, NY, USA, 2022. Association for Computing Machinery.
- [25] Christopher Chamberland, Guanyu Zhu, Theodore J Yoder, Jared B Hertzberg, and Andrew W Cross. Topological and subsystem codes on low-degree graphs with flag qubits. *Physical Review X*, 10(1):011022, 2020.
- [26] Ben W Reichardt. Fault-tolerant quantum error correction for steane’s seven-qubit color code with few or no extra qubits. *Quantum Science and Technology*, 6(1):015007, nov 2020.
- [27] Kristina R Colladay and Erich J Mueller. Rewiring stabilizer codes. *New Journal of Physics*, 20(8):083030, 2018.
- [28] Peter W Shor. Fault-tolerant quantum computation. In *Proceedings of 37th conference on foundations of computer science*, pages 56–65. IEEE, 1996.
- [29] Andrew M Steane. Active stabilization, quantum computation, and quantum state synthesis. *Physical Review Letters*, 78(11):2252, 1997.
- [30] Emanuel Knill. Quantum computing with realistically noisy devices. *Nature*, 434(7029):39–44, 2005.
- [31] Leonardo De Moura and Nikolaj Bjørner. Z3: An efficient smt solver. In *International conference on Tools and Algorithms for the Construction and Analysis of Systems*, pages 337–340. Springer, 2008.
- [41] David P DiVincenzo and Panos Aliferis. Effective fault-tolerant quantum computation with slow measurements. *Physical review letters*, 98(2):020501, 2007.
- [32] Chu Min Li and Felip Manyà. Maxsat, hard and soft constraints. In *Handbook of satisfiability*, pages 903–927. IOS Press, 2021.
- [33] Shilin Huang and Kenneth R Brown. Between shor and steane: A unifying construction for measuring error syndromes. *Physical review letters*, 127(9):090505, 2021.
- [34] Shilin Huang and Kenneth R Brown. Constructions for measuring error syndromes in calderbank-shor-steane codes between shor and steane methods. *Physical Review A*, 104(2):022429, 2021.
- [35] Yu Tomita and Krysta M Svore. Low-distance surface codes under realistic quantum noise. *Physical Review A*, 90(6):062320, 2014.
- [36] Noah Shutty and Christopher Chamberland. Decoding merged color-surface codes and finding fault-tolerant clifford circuits using solvers for satisfiability modulo theories. *Physical Review Applied*, 18(1):014072, 2022.
- [37] Chin Yang Lee. An algorithm for path connections and its applications. *IRE transactions on electronic computers*, (3):346–365, 1961.
- [38] Lingling Lao and Carmen G. Almudever. Fault-tolerant quantum error correction on near-term quantum processors using flag and bridge qubits. *Phys. Rev. A*, 101:032333, Mar 2020.
- [39] Daniel Gottesman. *Stabilizer codes and quantum error correction*. California Institute of Technology, 1997.
- [40] David Poulin. Stabilizer formalism for operator quantum error correction. *Physical review letters*, 95(23):230504, 2005.
- [42] Austin G Fowler, Matteo Mariantoni, John M Martinis, and Andrew N Cleland. Surface codes: Towards practical large-scale quantum computation. *Physical Review A*, 86(3):032324, 2012.
- [43] Ian P Gent and Peter Nightingale. A new encoding of alldifferent into sat. In *International Workshop on Modelling and Reformulating Constraint Satisfaction*, volume 3, pages 95–110, 2004.
- [44] Rui Chao and Ben W Reichardt. Quantum error correction with only two extra qubits. *Physical review letters*, 121(5):050502, 2018.
- [45] Jiongzhi Zheng, Kun He, Jianrong Zhou, Yan Jin, Chumin Li, and Felip Manyà. Incorporating multi-armed bandit with local search for maxsat. *ArXiv*, abs/2211.16011, 2022.
- [46] Alexey Ignatiev, Antonio Morgado, and Joao Marques-Silva. PySAT: A Python toolkit for prototyping with SAT oracles. In *SAT*, pages 428–437, 2018.
- [47] Craig Gidney. Stim: a fast stabilizer circuit simulator. *Quantum*, 5:497, 2021.
- [48] Oscar Higgott. Pymatching: A python package for decoding quantum codes with minimum-weight perfect matching. *ACM Transactions on Quantum Computing*, 3(3):1–16, 2022.
- [49] Clare Horsman, Austin G Fowler, Simon Devitt, and Rodney Van Meter. Surface code quantum computing by lattice surgery. *New Journal of Physics*, 14(12):123011, 2012.
- [50] Panos Aliferis and Andrew W Cross. Subsystem fault tolerance with the bacon-shor code. *Physical review letters*, 98(22):220502, 2007.
- [51] Maxime A Tremblay, Nicolas Delfosse, and Michael E Beverland. Constant-overhead quantum error correction with thin planar connectivity. *Physical Review Letters*, 129(5):050504, 2022.